Numerical Simulations of Methane Aromatization with and without a Ceramic Hydrogen Separation Membrane

Zuoan Li*[1], Christian Kjølseth[2], Selene Hernandez Morejudo[3], and Reidar Haugsrud[1]
[1] University of Oslo, Department of Chemistry, FERMiO, Gaustadalleen 21, NO-0349 Oslo, Norway
[2] Protia AS, Gaustadalleen 21, NO-0349 Oslo, Norway
[3] University of Oslo, Department of Chemistry, InGAP, Sem Sælandsvei 26, NO-0371 Oslo, Norway
*Corresponding author: zuoan.li@smn.uio.no

Abstract: Methane dehydroaromatization is promising for direct production of valuable industrial products such as benzene and hydrogen via the reaction $6CH_4 = C_6H_6 + 9H_2$. By removing hydrogen from the product stream, the yield of benzene can be increased. In the present investigation, reaction kinetics, mass transport and fluid dynamics have been coupled to simulate effects of various parameters such as flow rate and temperature on the reaction yield. Moreover, effects of coking on the reaction is also explored.

Keywords: methane aromatization, catalytic reactor, hydrogen separation membrane, coking effect

1. Introduction

Non-oxidative reaction of methane dehydroaromatization over cation-modified zeolites has been attracting growing attention due to a potential means for producing high valuable products such as aromatics and hydrogen via the reaction $6CH_4 = C_6H_6 + 9H_2$ [1], as schematically shown in Fig. 1. Many studies have been focused on catalysts screening and characterization, and elementary thermodynamic steps of the reaction [2, 3]. However, little attention has been paid to fluid dynamics such as flow rate and pressure gradient, which are important for an industrial application.

The highly endothermic nature of methane conversion to aromatics (e.g., 600 kJ/mol at 900 K), however, results in very low equilibrium conversions of methane and yields of benzene. One way to improve the methane dehydroaromatization process is the elimination of the hydrogen formed during the reaction, which inhibits the forward rates of the reaction. Thus, the use of a membrane reactor with continuous H_2 removal during the reaction could be possible to change the thermodynamic limitations and increase the methane conversion. Ceramic proton conductors based on $Ln_{6-x}WO_{12-\delta}$ (Ln = rare earths) have shown high chemical stability in carbon-containing atmospheres [4, 5] and can be used to transport the produced hydrogen in the reactor via ambipolar transport of protons and electrons. However, coupling of methane aromatization reaction and hydrogen removal poses significant design and optimization issues, which need to be solved numerically.

In the present contribution, COMSOL Multiphysics 4.2 has been used to study the methane dehydroaromatization. First, a fixed catalyst bed reactor has been simulated in order to verify the model used, and then a hydrogen separation membrane has been coupled to study the effect of hydrogen removal. Moreover, the influence of various parameters, such as space velocity, temperature, and hydrogen transport properties, on the reaction, have also been studied.

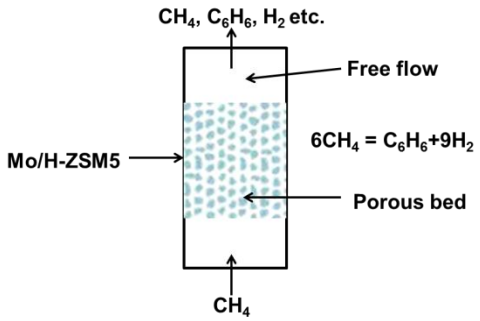

Figure 1. Schematic illustration of a catalytic reactor for the methane aromatization.

2. Two-dimensional model approaches

For a tubular reactor, an axisymmetric geometry can been used to reduce the computation time. The catalyst reactor can be divided into two free flow regions and one porous catalyst bed region, where the methane aromatization takes place (cf. Fig. 1). Detailed chemical reactions are as follows.

2.1 Reaction kinetics

Using Mo/H-ZSM5 as catalysts, two main independent chemical reactions are

$$6CH_4 = C_6H_6 + 9H_2 \quad (1)$$

$$CH_4 = C + 2H_2 \quad (2)$$

Although Reaction 2 has often been neglected, it is necessary to include it here to study potential effects of coking. The rate equations for these two reactions were optimized according to experimental data from 913 to 973 K, and described by the following Langmuir-Hinshelwood expressions [6]:

$$r_1 = \frac{k_1 f_{CH_4}^6 \left(1 - \frac{f_{C_6H_6} f_{H_2}^9}{K_{R_1} f_{CH_4}^6}\right)}{\left(1 + K_{CH_4} f_{CH_4} + K_{H_2} f_{H_2} + K_{C_6H_6} f_{C_6H_6}\right)^6} \quad (3)$$

$$r_2 = \frac{k_2 f_{CH_4} \left(1 - \frac{f_{H_2}^2}{K_{R_2} f_{CH_4}}\right)}{1 + K_{CH_4} f_{CH_4} + K_{H_2} f_{H_2} + K_{C_6H_6} f_{C_6H_6}} \quad (4)$$

where f_i is the fugacity of component i; K_{R1} and K_{R2} is the equilibrium constant of reactions 1 and 2, respectively, which can be calculated from thermodynamic data [7]; k_1 and k_2 are the rate constants of Reactions 1 and 2, respectively; K_i is the adsorption equilibrium constant of component i. The following kinetic parameters are used for the present simulations.

$$k_1 = 8.1283 \times 10^{-3} \exp\left(-\frac{2.0909 \times 10^5}{R}\left(\frac{1}{T} - \frac{1}{943.15}\right)\right) \quad (5)$$

$$k_2 = 2.3252 \times 10^{-3} \exp\left(-\frac{1.2096 \times 10^5}{R}\left(\frac{1}{T} - \frac{1}{943.15}\right)\right) \quad (6)$$

$$K_{CH_4} = \exp\left(-1.1963 - 1.3209 \times 10^2\left(\frac{1}{T} - \frac{1}{943.15}\right)\right) \quad (7)$$

$$K_{H_2} = \exp\left(1.6736 + 1.5796 \times 10^3\left(\frac{1}{T} - \frac{1}{943.15}\right)\right) \quad (8)$$

$$K_{C_6H_6} = \exp\left(-9.09 + 1.177 \times 10^5\left(\frac{1}{T} - \frac{1}{943.15}\right)\right) \quad (9)$$

2.2 Mass transport

Since the concentration of C_6H_6 and H_2 in the catalytic bed is high [1, 2, 6], the transport of concentrated species i including Maxwell-Stefan diffusion and convection equations has to be applied

$$\nabla\left(\rho\omega_i u - \rho\omega_i \sum_{j=1}^{n} \tilde{D}_{ij}\left(\nabla x_j + \left(x_j - \omega_j\right)\frac{\nabla p}{p}\right)\right) = R_i \quad (10)$$

where ρ denotes the density (kg/m^3) of the fluid which can be calculated by ideal gas law, u is the velocity of the fluid (m/s), p is the pressure (Pa), ω_i is the mass fraction of species i, x_j is the molar fraction of species j, and $\tilde{D}_{ij}$ is the ij component of the multicomponent Fick diffusivity (m^2/s), which is strongly dependent on the composition and given by [8, 9]

$$\tilde{D}_{11} = \frac{\frac{(\omega_2 + \omega_3)^2}{x_1 D_{23}} + \frac{\omega_2^2}{x_2 D_{13}} + \frac{\omega_3^2}{x_3 D_{12}}}{\frac{x_1}{D_{12} D_{13}} + \frac{x_2}{D_{12} D_{23}} + \frac{x_3}{D_{13} D_{23}}} \quad (11)$$

$$\tilde{D}_{12} = \frac{\frac{\omega_1(\omega_2 + \omega_3)}{x_1 D_{23}} + \frac{\omega_2(\omega_1 + \omega_3)}{x_2 D_{13}} - \frac{\omega_3^2}{x_3 D_{12}}}{\frac{x_1}{D_{12} D_{13}} + \frac{x_2}{D_{12} D_{23}} + \frac{x_3}{D_{13} D_{23}}} \quad (12)$$

where D_{ij} is the Maxwell-Stefan diffusivity (m^2/s), and can be calculated with an empirical equation based on the kinetic gas theory [10]:

$$\boldsymbol{D_{ij}} = \boldsymbol{k}\frac{\boldsymbol{T}^{1.75}}{\boldsymbol{p}\left(\boldsymbol{v}_i^{1/3}+\boldsymbol{v}_j^{1/3}\right)}\left[\frac{1}{\boldsymbol{M}_i}+\frac{1}{\boldsymbol{M}_j}\right]^{1/2} \quad (13)$$

where k is a constant with the value 3.16×10^{-8} Pa m^2/s, M_i is the molar mass of species i (kg/mol), and v_i equals the molar diffusion volume of species i (m^3/mol).

To calculate R_i in Eq. 10, reaction kinetics in Section 2.1 must be coupled and the following relations can be obtained:

$$R_{\mathrm{CH_4}} = -6r_1 - r_2 \quad (14)$$

$$R_{\mathrm{C_6H_6}} = r_1 \quad (15)$$

$$\boldsymbol{R}_{\mathrm{H_2}} = 9\boldsymbol{r}_1 + 2\boldsymbol{r}_2 \quad (16)$$

The boundary condition at the inlet is the weight fraction of each species: 1 for methane and 0 for other species. At the outlet, the convective flux dominates the mass transport

$$\mathbf{n}\cdot\left(-\rho\omega_i\sum_{j=1}^{n}\tilde{\boldsymbol{D}}_{ij}\left(\nabla\boldsymbol{x}_j+\left(\boldsymbol{x}_j-\omega_j\right)\frac{\nabla\boldsymbol{p}}{\boldsymbol{p}}\right)\right)=0 \quad (17)$$

This implies that the concentration gradient in the direction perpendicular to the outlet boundary is negligible, which is common for tubular reactors with a high degree of transport by convection in the direction of the main reactor axis.

2.3 Momentum transport

Fluids in two free flow regions are described by the Navier-Stokes equation:

$$-\eta\nabla^2\boldsymbol{u}+\nabla\boldsymbol{p} = -\rho\boldsymbol{u}\cdot\nabla\boldsymbol{u} \quad (18)$$

where η denotes the dynamic viscosity (Pa s) and is approximated to that of methane due to being the main component in the fluid, and the other terms have the same meanings as defined in Eq. 10. In the porous catalyst region, flow can be described by the Brinkman equation as

$$-\frac{\eta}{\varepsilon_p}\nabla^2\boldsymbol{u}+\nabla\boldsymbol{p} = -\frac{\eta}{\kappa}\boldsymbol{u} \quad (19)$$

where ε_p is the porosity of the catalyst bed, and κ is the permeability of the catalyst porous media. For the sake of simplicity, the fluid viscosity is often assumed to be the same as that in free flow regions [11]. The porosity and permeability are two key factors that govern the fluid flow in the porous region. Using the Carman-Kozeny model [12], the permeability for a packed-bed with randomly distributed spherical particles can be expressed as

$$\kappa = \frac{\boldsymbol{d}_p^2\varepsilon_p^3}{150(1-\varepsilon_p)^2} \quad (20)$$

where d_p is the particle size of the catalyst.

At the inlet, the boundary condition is set to the velocity of the fluid, which can be calculated through the flow rate and cross sectional area of the reactor. At the outlet, the pressure is set to 1 atm unless the calculation aims to study the effect of pressure.

2.4 Hydrogen permeation

When a hydrogen separation membrane is applied to the catalyst reactor, the hydrogen produced inside the reactor can be removed by pumping, flushing or reaction with oxidizing gas as illustrated in Fig. 2.

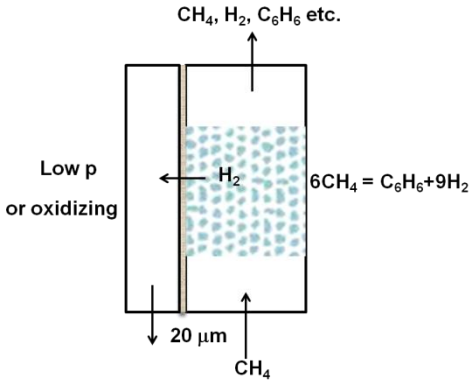

Figure 2. Schematic illustration of a catalytic membrane reactor.

Here, a dense ceramic mixed proton electron conductor based on $Ln_{6-x}WO_{12-\delta}$ (Ln = rare earths) is chosen as the hydrogen separation membrane due to its high stability, 100% hydrogen selectivity, and low cost as compared to Pd-based alloys [4, 5, 13]. Ambipolar transport of proton and electron gives a net flux of hydrogen [13]:

$$j_{H_2} = \frac{-RT}{4F^2L} \int_{\text{Reactor}}^{\text{Permeate}} \sigma_{H^+} t_{e^-} d\ln p_{H_2} \quad (21)$$

where L is the thickness of the membrane, σ_{H^+} is the proton conductivity, t_{e^-} is the transference number of electrons, and the other terms have their usual meanings. To simplify, we have assumed that the material is either predominated by electronic ($t_{e^-} \approx 1$) or proton conduction ($t_{H^+} \approx 1$) and that the conductivity of both charge carriers is proportional to $p_{H_2}^{1/2}$. Thereby the above equation can be integrated yielding

$$j_{H_2} = \frac{-RT\sigma_0}{2F^2L}\left[\left(p_{H_2}^{P}\right)^{1/2} - \left(p_{H_2}^{R}\right)^{1/2}\right] \quad (22)$$

where σ_0 is the conductivity (either proton or electron) at standard hydrogen pressure (1 atm). Due to high flow or oxidizing condition at the permeate side, the hydrogen partial pressure at the permeate side is much lower than that in the catalytic reactor. Thus, Eq. 22 can be further simplified to

$$j_{H_2} = \frac{RT\sigma_0}{2F^2L} \times \left(p_{H_2}^{R}\right)^{1/2} \quad (23)$$

When the conductivity is independent of p_{H_2}, the integration of Eq. 21 yields

$$j_{H_2} = \frac{-RT\sigma_0}{4F^2L}\left[\ln\left(p_{H_2}^{P}\right) - \ln\left(p_{H_2}^{R}\right)\right] \quad (24)$$

In this case, the flux will be determined by the ratio of p_{H_2} at both sides; the lower the p_{H_2} at the permeate side, the higher the hydrogen flux. Since it is easier to achieve low p_{H_2} at the permeate side by flushing with high flow or reaction with oxidizing gas than increase the conductivity of the membrane, this may provide us a way to select suitable membrane materials.

3. Results and discussion

3.1 Influence of flow rate, temperature and pressure

To test the model parameters, the molar fraction of H_2 and C_6H_6 at the outlet was first calculated and compared to experimental results at same temperatures and with a same space velocity. As evident from Fig. 3 a and b the agreement is acceptable, verifying the validity of the models suggested in this work.

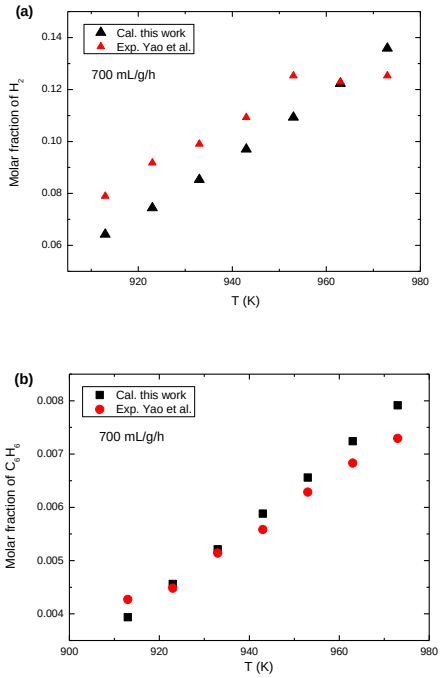

Figure 3. Comparison of the formed H_2 and C_6H_6 at the outlet between experiments [6] and simulations.

Fig. 4 demonstrates that the conversion rate of methane increases with increasing temperature and decreasing space velocity. It is worth noting that the conversion rate increases significantly by reducing the space velocity from 1500 to 700 mL/g/h, but that the difference between 1500 and 2100 mL/g/h is much smaller. This is instructive when choosing a suitable flow rate for a specific

industrial requirement. Again we see that the simulation reproduces the experimental data nicely. As the pressure at the outlet increases, the conversion rate decreases significantly as shown in Fig. 5. This may be due to thermodynamic limitations of the reactions.

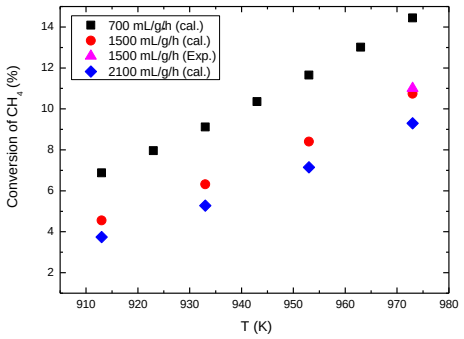

Figure 4. Conversion rate of methane as a function of temperature under various space velocities.

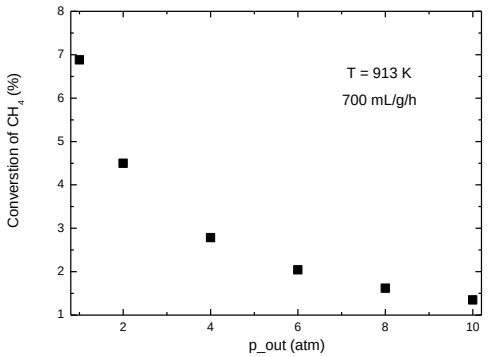

Figure 5. Conversion rate of methane as a function of pressure at the outlet.

3.2 Impact of hydrogen removal

To study the effect of extracting hydrogen, a 20 μm $Ln_{6-x}WO_{12-\delta}$ based membrane has been included in the model. Although thinner membranes definitely increase the hydrogen flux (see Eqs. 21-24), micron-scale membranes on porous supports are challenging for fabrication and material stability may as well become an issue due to potential kinetic demixing or decomposition [14]. Since the concentration of charge carriers limiting hydrogen transport in $Ln_{6-x}WO_{12-\delta}$ is usually dependent on p_{H_2}, Eq. 23 rather than Eq. 24 was selected for the simulation. By assuming that only one charge carrier limits the hydrogen flux, Fig. 6 presents simulations of how the conductivity, σ_0, of a 20 μm thick membrane affects the conversion rate at 913 and 973 K. There is no significant increase in the conversion rate until the conductivity reaches value of 10^{-3} S/cm above which the efficiency of the membrane gradually increases. More methane is converted to benzene as hydrogen is extracted, but this effect is not so significant at 913K as compared to 973 K due to kinetic limitations. Since the hydrogen flux is proportional to σ_0/L according to Eq. 23, the obtained value of σ_0/L = 0.5 S/cm^2 where a membrane starts to take effect, can be easily applied to membranes with different thicknesses.

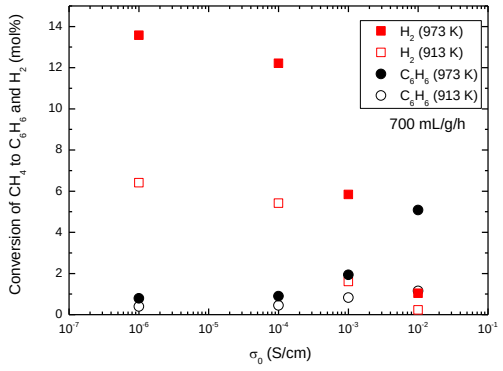

Figure 6. Conversion rate of CH_4 to C_6H_6 and H_2 vs. conductivity of the membrane with 20 μm thick.

Although removing hydrogen increases the yield of benzene, coking can not be ignored (see Reaction 2). Fig. 7 reveals that the more hydrogen is removed, the more coke is produced, in particular at high temperature. Coke can cause the catalysts to be poisoned via either active site suppression or pore blocking [15], resulting in a decreasing conversion rate of methane as time goes, especially for a catalytic membrane reactor [16]. The deactivation of catalysts may be weakened by diluting catalysts, and this will cause a change in the fluid dynamics. To get a

better understanding of coking, time-dependent simulations is called for in the future.

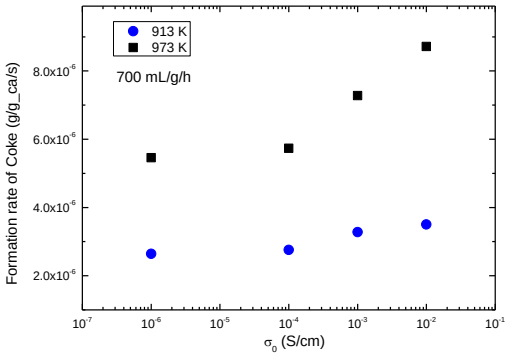

Figure 7. Coke formation rate vs. conductivity of the membrane with 20 μm thick.

4. Conclusion

Reaction kinetics, mass transport and fluid dynamics have been coupled to simulate methane aromatization. The simulated results have revealed that higher conversion rates of methane can be achieved by decreasing space velocity and pressure, and increasing temperature. A series of suitable parameters has been determined depending on the purpose of the application. To increase the yield of benzene by removing hydrogen in the reactor via a hydrogen separation membrane, the value of σ_0/L must be higher than 0.5 S/cm^2 for a space velocity of 700 mL/g/s and above 913 K. With the removal of hydrogen, the formation rate of coke is becoming more significant and must be treated carefully.

5. Acknowledgement

Financial supports from the Research Council of Norway (RCN) under the project *Intensified Conversion of Alkanes to Aromatics and Olefins Using Integrated Catalyst/Membrane Reactor (ICOR) (210418), Nonoxidative Methane Activation by Co-conversion of Methane over Metal Containing Zeolite Catalysts (182537),* and *Kinetics of High-Temperature Oxide Ion and Proton Conductors (KINOXPRO) (RENERGI 190901/S60)* are gratefully acknowledged.

6. References

1. Z.R. Ismagilov, E.V. Matus, and L.T. Tsikoza, Direct converison of methane on Mo/ZSM-5 catalysts to produce benzene and hydrogen: achievements and perspectives, *Energy Environ. Sci.*, **1**, 526-541(2008).
2. Y. Xu, and L. Lin, Recent advances in methane dehydro-aromatization over transition metal ion-modified zeolite catalysts under non-oxidative conditions, *J. Appl. Catal., A*, **188**, 53-67 (1999).
3. A.M. Dean, Detailed kinetic modelling of autocatalysis in methane pyrolysis, *J. Phys. Chem.*, **94**, 1432-1439 (1990).
4. R. Haugsrud, Defects and transport properties in Ln_6WO_{12} (Ln=La, Nd, Gd, Er), *Solid State Ionics*, **178**, 555-560 (2007).
5. R. Haugsrud, and C. Kjølseth, Effects of protons and acceptor substitution on the electrical conductivity of La_6WO_{12}, *J. Phys. Chem. Solids*, **69**, 1758-1765 (2008).
6. B. Yao, J. Chen, D. Liu and D. Fang, Intrinsic kinetics of methane aromatization under non-oxidative conditions over modified Mo/HZSM-5 catalysts, *Journal of Natural Gas Chemistry*, **17**, 64-68 (2008)
7. R.H. Perry, and D.W. Green, *Perry's Chemical Engineers' Handbook*, 7th ed., McGraw-Hill Professional, 1997.
8. R. Bird, W. Stewart, and E. Lightfoot, *Transport Phenomena*, 2nd ed., John Wiley & Sons, 2002.
9. C.F. Curtiss and R.B. Bird, Multicomponent Diffusion, *Ind. Eng. Chem. Res.*, **38**, 2515-2522 (1999).
10. J.A. Wesselingh and R. Krishna, *Mass Transfer in Multicomponent Mixer*, Delft University Press, (2000).
11. R.Y. Chein, L.C. Chen, Y.C. Chen and J.N. Chung, Heat transfer effects on the methanol-steam reforming with partially filled catalyst layers, *International Journal of Hydrogen Energy*, **34**, 5398-5408 (2009).
12. D.A. Nield, and A. Bejan, *Convection in porous media*, Springer Science-Business Media, New York (2006).
13. T. Norby, and R. Haugsrud, *Membranes for Energy Conversion*, Wiley-VCH Verlag GmbH & Co. KGaA, pp.169-216 (2008).
14. M. Martin, Materials in thermodynamic potential gradients, *J. Chem. Thermodynamics*, **35**, 1291-1308 (2003).

15. A. De Lucas, P. Canizares, A. Duran, P. Sanchez and M.T. Garcia, Modified W/HZSM-5 catalysts: structure and catalytic properties, *Applied Catalyst A: General*, **156**, 299-317 (1997).
16. O. Rival, B.P.A. Grandjean, C. Guy, A. Sayari, and F. Larachi, Oxygen-free methane aromatization in a catalytic membrane reactor, *Ind. Eng. Chem. Res.*, **40**, 2212-2219 (2001).